

Nitrogen Dioxide Pollution as a Signature of Extraterrestrial Technology

RAVI KOPPARAPU ¹, GIADA ARNEY,¹ JACOB HAQQ-MISRA ², JACOB LUSTIG-YAEGER ³ AND
GERONIMO VILLANUEVA ¹

¹*NASA Goddard Space Flight Center
8800 Greenbelt Road
Greenbelt, MD 20771, USA*

²*Blue Marble Space Institute of Science,
Seattle, WA, USA*

³*Johns Hopkins University Applied Physics Laboratory,
Laurel, MD 20723, USA*

Submitted to ApJ

ABSTRACT

Nitrogen dioxide (NO₂) on Earth today has biogenic and anthropogenic sources. During the COVID-19 pandemic, observations of global NO₂ emissions have shown significant decrease in urban areas. Drawing upon this example of NO₂ as an industrial byproduct, we use a one-dimensional photochemical model and synthetic spectral generator to assess the detectability of NO₂ as an atmospheric technosignature on exoplanets. We consider cases of an Earth-like planet around Sun-like, K-dwarf and M-dwarf stars. We find that NO₂ concentrations increase on planets around cooler stars due to less short-wavelength photons that can photolyze NO₂. In cloud-free results, present Earth-level NO₂ on an Earth-like planet around a Sun-like star at 10pc can be detected with SNR ~ 5 within ~ 400 hours with a 15 meter LUVUOIR-like telescope when observed in the $0.2 - 0.7\mu\text{m}$ range where NO₂ has a strong absorption. However, clouds and aerosols can reduce the detectability and could mimic the NO₂ feature. Historically, global NO₂ levels were 3x higher, indicating the capability of detecting a 40-year old Earth-level civilization. Transit and direct imaging observations to detect infrared spectral signatures of NO₂ on habitable planets around M-dwarfs would need several 100s of hours of observation time, both due to weaker NO₂ absorption in this region, and also because of masking features by dominant H₂O and CO₂ bands in the infrared part of the spectrum. Non-detection at these levels could be used to place upper limits on the prevalence of NO₂ as a technosignature.

Keywords: Exoplanet atmospheric composition, technosignatures

1. INTRODUCTION

Over the last 25 years, more than 4000 exoplanets have been discovered¹ from both ground and space-based surveys. We are now entering into an era of exoplanet atmospheric characterization, with the soon to be launched James Webb Space Telescope (*JWST*), Atmospheric Remote-sensing Infrared Exoplanet Large-survey (*ARIEL*) space telescope, and large ground-based observatories such as the European Extremely Large Telescope (*E-ELT*), the Thirty Meter Telescope (*TMT*), and the Giant Magellan Telescope (*GMT*). The first detection of an exoplanet atmosphere was on a gas giant planet, HD 209458b, in 2001 ([Charbonneau et al. 2002](#)). Since then, atmospheres have been detected on exoplanets spanning a wide range of planetary parameter space, and observers are continuing to push the limits towards smaller worlds ([Tsiaras et al. 2019](#); [Benneke et al. 2019](#)). The ongoing discovery of exoplanet atmospheres has raised the prospect of eventually identifying potentially habitable planets, as well as the possibility of finding one that

Corresponding author: Ravi Kopparapu
ravikumar.kopparapu@nasa.gov

¹ <https://exoplanetarchive.ipac.caltech.edu/>

may also be inhabited. As a result, the characterization and detection of “biosignatures,”—remote observations of atmospheric spectral features that could potentially indicate signs of life on an exoplanet—has received recent attention as an area of priority for astrobiology² (Seager et al. 2012; Kaltenegger 2017; Schwieterman et al. 2018; Meadows et al. 2018; Catling et al. 2018; Walker et al. 2018; Fujii et al. 2018; O’Malley-James & Kaltenegger 2019; Lammer et al. 2019; Grenfell 2017).

Similar to biosignatures, “technosignatures” refer to any observational manifestations of extraterrestrial technology that could be detected or inferred through astronomical searches. As discussed in the 2018 NASA technosignatures workshop report (Technosignatures Workshop Participants 2018): “Searches for technosignatures are logically continuous with the search for biosignatures as part of astrobiology. As with biosignatures, one must proceed by hypothesizing a class of detectable technosignatures, motivated by life on Earth, and then designing a search for that technosignature considering both its detectability and its uniqueness.” Although the science of atmospheric technosignatures is less developed compared to atmospheric biosignatures, a wide class of possible technosignatures have been suggested in the literature that include waste heat (Dyson 1960; Wright et al. 2014; Kuhn & Berdyugina 2015; Carrigan Jr. 2009), artificial illumination (Schneider 2010; Loeb & Turner 2012; Kipping & Teachey 2016), artificial atmospheric constituents (Schneider 2010; Lin et al. 2014; Stevens et al. 2016), artificial surface constituents (Lingam & Loeb 2017), stellar “pollution” (Shklovskii & Sagan 1966; Whitmire & Wright 1980; Stevens et al. 2016), non-terrestrial artifacts (Bracewell 1960; Freitas Jr & Valdes 1980; Rose & Wright 2004; Haqq-Misra & Kopparapu 2012), and megastructures (Dyson 1960; Arnold 2005; Forgan 2013; Wright et al. 2016). This breadth of topics reflects the scope of possibilities for detecting plausible technosignatures, although the sophistication of technosignature science remains in its infancy compared to the rapidly evolving field of biosignatures (Wright 2019; Haqq-Misra et al. 2020).

The history of life on Earth provides a starting point in the search for biosignatures on exoplanets (Krissansen-Totton et al. 2018; Pallé 2018), with the various stages of Earth’s evolution through the Hadean (4.6 - 4 Gyr), Archean (4 - 2.5 Gyr), Proterozoic (2.5 - 0.54 Gyr), and Phanerozoic (0.54 Gyr - present) eons representing atmospheric compositions to use as examples of spectral signatures of an inhabited planet. The use of Earth’s history as an example does not imply that these biosignatures will necessarily be the most prevalent in the galaxy, but instead this approach simply represents a place to begin based on the one known example of life. By extension, the search for technosignatures likewise can consider Earth’s evolution into the Anthropocene epoch (Crutzen 2006; Lewis & Maslin 2015; Frank et al. 2017) as a template for future observing campaigns that seek to detect evidence of extraterrestrial technology. For instance, Lin et al. (2014) discussed the possibility of detecting tetrafluoromethane (CF_4) and trichlorofluoromethane (CCl_3F) signatures in the atmospheres of transiting Earth-like planets around white dwarfs with JWST, which could be detectable if these compounds are present at 10 times the present Earth level. These chlorofluorocarbons (CFCs) are produced by industrial processes on Earth, so their detection in an exoplanet atmosphere could be strong evidence for the presence of extraterrestrial technology. This approach does not insist that CFCs or other industrial gases found on Earth will necessarily be the most prevalent technosignature in the galaxy, but it represents a place to begin defining observables and plausible concepts for technosignatures based upon the one known example of technological civilization.

In this study, we explore the possibility of NO_2 as an atmospheric technosignature. Some NO_2 on Earth is produced as a byproduct of combustion, which suggests the possibility of scenarios in which larger-scale production of NO_2 is sustained by more advanced technology on another planet. Detecting high levels of NO_2 at levels above that of non-technological emissions found on Earth could be a sign that the planet may host active industrial processes. In section 2, we describe the production reactions of NO_2 and use a 1-dimensional photochemical model to obtain self-consistent mixing ratio profiles of nitrogen oxide compounds, on a planet orbiting a Sun-like star, a K6V spectral type ($T_{eff} = 4600\text{K}$), and the two M-dwarf stars AD Leo ($T_{eff} = 3390\text{K}$) and Proxima Centauri ($T_{eff} = 3000\text{K}$). Using these photochemical results, in section 3 we calculate the observability of strongest NO_2 features between $0.2 - 0.7\mu\text{m}$ and between $1 - 10\mu\text{m}$ using a spectral generation model to produce geometric albedo and transit spectra of planets with various facilities like LUVUOIR-15m, JWST and OST. In section 4, we discuss the implications of these observations, concluding in section 5.

2. PRODUCTION OF NITROGEN DIOXIDE

² <https://www.nationalacademies.org/our-work/astrobiology-science-strategy-for-the-search-for-life-in-the-universe>

Nitrogen oxides ($\text{NO}_x = \text{NO} + \text{NO}_2$) are among the main pollutants in industrialized locations on the globe. The non-anthropogenic pathways for the production of NO_x can be either due to emission from soils and wildfires, or produced in the troposphere by lightning.³ The primary biogenic source of NO_x is bacteria in soil through nitrification (i.e bacteria converting ammonia to nitrite and nitrate compounds), or denitrification (process of reducing nitrate and nitrite to gaseous forms of nitrogen such as N_2 or N_2O). The estimated worldwide biogenic and lightning emissions of NO_x compounds are ~ 10.6 Tera gram per year as N (Tg(N) yr^{-1} , (Table 1, [Holmes et al. \(2013\)](#)). Lightning contributes about 5 Tg(N) yr^{-1} , which translates to $6 \times 10^8 \text{ NO molecules/cm}^2/\text{s}$ ([Harman et al. 2018](#)).

On the other hand, NO_x compounds are also emitted from anthropogenic sources of combustion processes such as vehicle emissions and fossil-fueled power plants. The role of this industrial production was noted during the COVID-19 pandemic, when global concentrations of NO_2 were observed to decrease between 20 – 40% over urban areas ([Bauwens et al. 2020](#)). Indeed, these emissions dominate the production of NO_x compounds in the troposphere more than the biogenic sources with an estimated rate of 32 Tg(N) yr^{-1} ([Holmes et al. 2013](#)). NO_2 poses harmful health effects that could cause impairment of lung function and respiratory problems ([Faustini et al. 2014a](#)). Typical concentrations of NO_2 range from 0.01 ppb (parts per billion) to ~ 5 ppb depending upon the urbanization with the higher number correlating to urban areas ([Lamsal et al. 2013](#)). The presence of NO_x in the lower troposphere leads to a complex chemistry that results in the formation of ozone (O_3), which is a harmful pollutant in the troposphere and a greenhouse gas. NO_x mixing ratios in excess of 10^{-7} would cause severe damage to the O_3 layer and could result in either a climatic warming or cooling, depending upon the amount of NO_2 present ([Kasting & Ackerman 1985](#)).

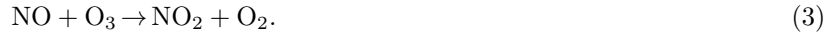
The sinks and sources for NO_2 in the troposphere ($\leq 20\text{km}$) are governed by the following reactions. NO_2 photolysis is dominant in the wavelength range of 290 – 420nm (See [Kraus & Hofzumahaus \(1998\)](#), Fig. 2). The lower limit is set by the available solar UV-intensity and the upper wavelength limit is determined by the fall-off in the photodissociation cross-section. This NO_2 photolysis produces ground state atomic oxygen, $\text{O}(^3\text{P})$, along with NO :



The $\text{O}(^3\text{P})$ then can combine with an oxygen molecule to form ozone,



which gets destroyed by reoxidizing nitric oxide to nitrogen dioxide:



NO also reacts with atomic oxygen (O) and the hydroperoxy radical (HO_2) to generate NO_2 ,



However, these production mechanisms of NO_2 are counteracted when NO_2 reacts again with atomic oxygen to recreate NO :



The above reactions just cycle between NO and NO_2 , so NO_x is conserved. However, NO_2 also reacts with the OH radical to form nitric acid (HNO_3), which eventually is removed from the atmosphere by rainout, which is a loss process for NO_x :



Reactions 3 and 6 form a catalytic cycle to destroy ozone with the net reaction,



³ The troposphere is the lowermost atmospheric layer from the surface up to 10-18 km, highest at the tropics and lowest near the poles during winter. The pressure and temperature decrease with altitude, with global averages of 289K and 1.013 millibar (mb) at the surface, and around 210K and 150 mb at a height of 15 km.

indicating that high stratospheric NO_x can lead to ozone depletion.

To study the steady-state abundances of NO_x compounds in Earth-like atmospheres, we used a 1-D photochemical model (described in Arney et al. 2016; Arney 2019), which is part of a coupled climate-photochemistry model called ‘Atmos.’⁴ The photochemical model is originally based on the one described in Kasting et al. (1979) and has been updated extensively over the years and applied to various planetary and exoplanetary conditions (e.g. Segura et al. 2005; Kopparapu et al. 2012; Domagal-Goldman et al. 2014; Harman et al. 2015, 2018; Lincowski et al. 2018). The model version used here has been updated to correct the deficiencies identified in Ranjan et al. (2020), and the public version of the model is planned to be updated. This model solves a set of nonlinear, coupled ordinary differential equations for the mixing ratios of all species at all heights using the reverse Euler method. The method is first order in time and uses second-order centered finite differences in space. The vertical grid has 200 altitude levels, ranging from 0 km (lower boundary) to 100 km (upper boundary). The version used here includes updates described in Lincowski et al. (2018) and includes 72 chemical species involved in 309 reactions to represent a modern Earth-like planet. We considered a Sun-like star, a K6V stellar spectral type, and two M-stars (AD Leo and Proxima Centauri) in this study. For the Sun-like star we used the Chance & Kurucz (2010) model; for the K6V star, we used the spectrum of HD 85512 from the Measurements of the Ultraviolet Spectral Characteristics of Low-mass Exoplanetary Systems (MUSCLES) treasury survey (France et al. 2016; Loyd et al. 2016; Youngblood et al. 2016); for AD Leo and Proxima Centauri, we used stellar spectra described in Segura et al. (2005) and Meadows et al. (2018), respectively. Planets around the other stars are placed at the Earth-equivalent flux distance.

For each Earth-like planet around its host star, we ran the model to steady state to obtain the mixing ratio profiles of all gaseous species, including NO₂. We have used a surface NO₂ molecular flux of 8.64×10^9 molecules/cm²/s as the standard Earth-level (1x) flux in our simulations. This number comes from converting the estimated rate of 32 Tg(N) yr⁻¹ anthropogenic NO_x compound emissions in the troposphere⁵ to the molecular flux. We also include a fixed biogenic flux of NO as 1.0×10^9 molecules/cm²/s, kept constant across all simulations. Because we do not increase the flux of NO alongside NO₂, our simulations may be regarded as somewhat conservative. Other fixed boundary conditions of N-bearing species include: a flux of 1.53×10^9 for N₂O, a mixing ratio of 0.78 for N₂, and fixed deposition velocities of 2.1×10^{-1} for HO₂NO₂ and HNO₃.

Results from our 1-D photochemical model are shown in Fig. 1, panel (a). This plot shows the NO₂ volume mixing ratio profiles of an Earth-like planet around four stellar spectral types we considered in this study: the Sun (blue), AD Leo (green), Proxima Centauri (black) and the K6V star (magenta). Two end member concentrations are shown: The standard Earth level flux of 8.64×10^9 molecules/cm⁻²/s (1x, solid curves), and a flux of 172×10^9 molecules/cm⁻²/s (20x, dashed curves). The corresponding stellar spectra are shown in the right panel (b), highlighting the wavelength region of strongest NO₂ absorption. As shown in this figure, the hotter stars provide more photons between 0.25 to 0.65 μm, which increases the rate of NO₂ photolysis (Eq. 1, and also Table 1).

However, photolysis is not the only important factor. As shown in Table 1 and Fig. 2, O₃ also plays a major role in determining NO₂ concentration. Panel (a) in Fig. 2 shows the O₃ mixing ratio profiles for various stars. For the Sun (blue), the O₃ concentration increases rapidly below ~ 20 km compared to other stars. O₃ participates in the dominant production reaction for NO₂, with the help of NO as shown in Table 1. Ideally, this should increase the concentration of NO₂ below 20 km. However, as shown in panel (b) of Fig. 2, photolysis of NO₂ due to photons of wavelengths between 0.29 – 0.42 μm that penetrate into the troposphere dominate the destruction of NO₂, decreasing its mixing ratio (See Fig. 1, panel a). While the photolysis rates generally increase for all stars below 20 km as shown in panel b of Fig. 2, it is the rate at which O₃ increases below this altitude that determines the slope of decrease in NO₂ in the troposphere for planets around different stars. While the rapid increase in O₃ is mostly negated by the rapid photolysis and consequent decrease of NO₂ below ~ 20km for Sun-like stars (blue solid in Figs. 1 and 2), for other stars the O₃ concentration increases only a little from the surface to the tropopause (black, green and magenta curves in Fig. 2). Consequently, the increasing slope of photolysis rate of NO₂ below ~ 20 km for these other stars slightly dominates (panel b), resulting in a *larger* decrease in the mixing ratio of NO₂ compared to a Sun-like star (panel a in Fig. 1).

As a result, the column integrated NO₂ abundance increases moving from hotter stars to cooler stars (Table 2). The absorption cross sections for NO₂ and other key gases are shown in Fig. 3. A Sun-like star produces more photons at

⁴ <https://github.com/VirtualPlanetaryLaboratory/atmos>

⁵ 32×10^{12} (gram/year) / $(1.67 \times 10^{-24}$ gram $\times 14 \times 4\pi(6.32 \times 10^6 m)^2 \times 365 \times 24 \times 3600s) \sim 8.64 \times 10^9$ molecules/cm²/s

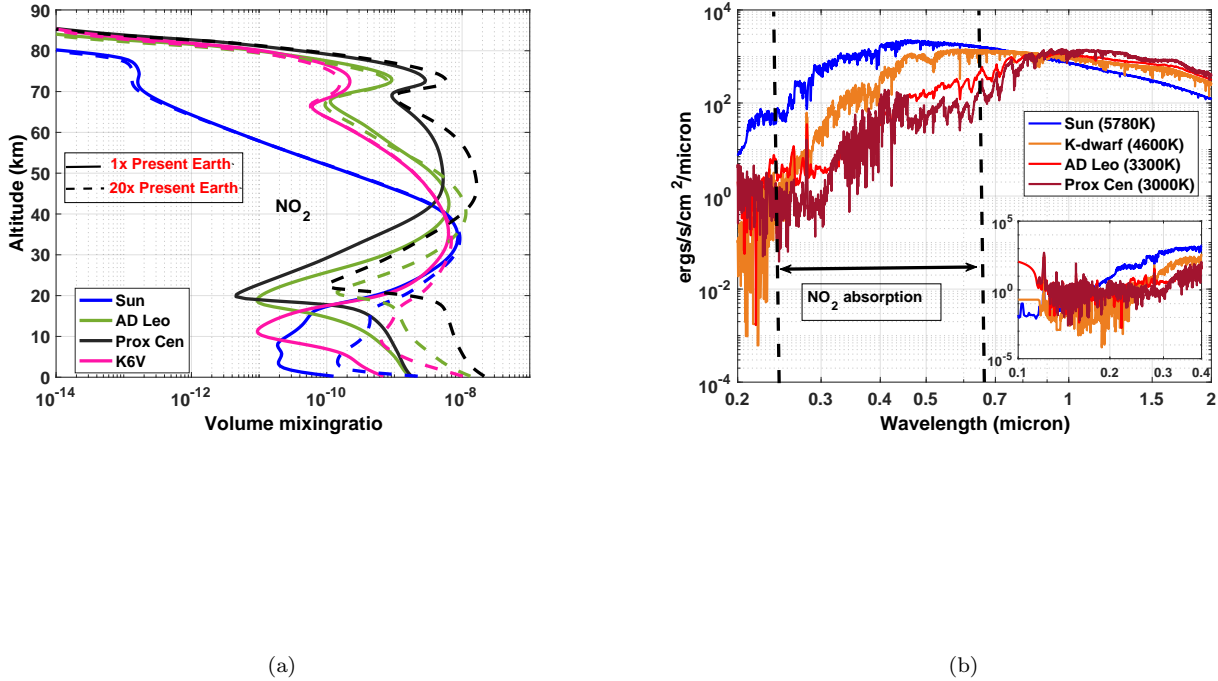


Figure 1. (a): Mixing ratio profiles of NO₂ around stars of different spectral types on an Earth-like planet with 1x (solid) and 20x (dashed) present Earth NO₂ fluxes. Below the troposphere (~ 20 km), NO₂ concentration is higher on planets around cooler stars compared to the Sun because the destruction of NO₂ is an order of magnitude more efficient around a Sun-like star due to the availability of photons of wavelength between 0.29 – 0.42 μ m that penetrate to the troposphere. See inset in panel b. (b) Spectral energy distribution of stellar spectral types used in this study, indicating wavelength region of strongest NO₂ absorption. The inset shows the UV/Visible region where NO₂ photolysis happens.

wavelengths where NO₂ is photolyzed (between 290 – 420nm), so the photolysis rates of NO₂ is higher for the planet around the Sun than for a planet around a cooler star (Table 1).

The result of all the dominant production and destruction reactions discussed above is that NO and NO₂ decrease with altitude until ~ 20 km, into the stratosphere. In the stratosphere, ozone can generate NO₂ with reactions with NO; ozone’s overlapping UV cross section with NO₂ also provides some UV shielding. At higher altitudes, above the ozone layer, photochemical processes, including NO₂ photolysis and reaction with OH radicals, draw down abundances. These reactions occur most markedly for the planet orbiting the Sun; NO₂ photolysis proceeds 1-2 orders of magnitude faster around the Sun compared to around the cooler stars. Reaction of NO₂ with OH to form HNO₃ occurs two orders of magnitude more efficiently around the Sun compared to the K6V star, and fully 4-6 orders of magnitude more efficiently around the Sun compared to the M dwarfs.

It is important to note that placing constraints on a planet’s NO₂ abundance from its spectrum would not definitively answer whether the NO₂ is biologically or abiotically produced. One would need to estimate the production rates required to produce the observed NO₂ abundance and evaluate whether abiotic sources alone can sustain the inferred production rate.

3. DETECTABILITY OF NITROGEN DIOXIDE

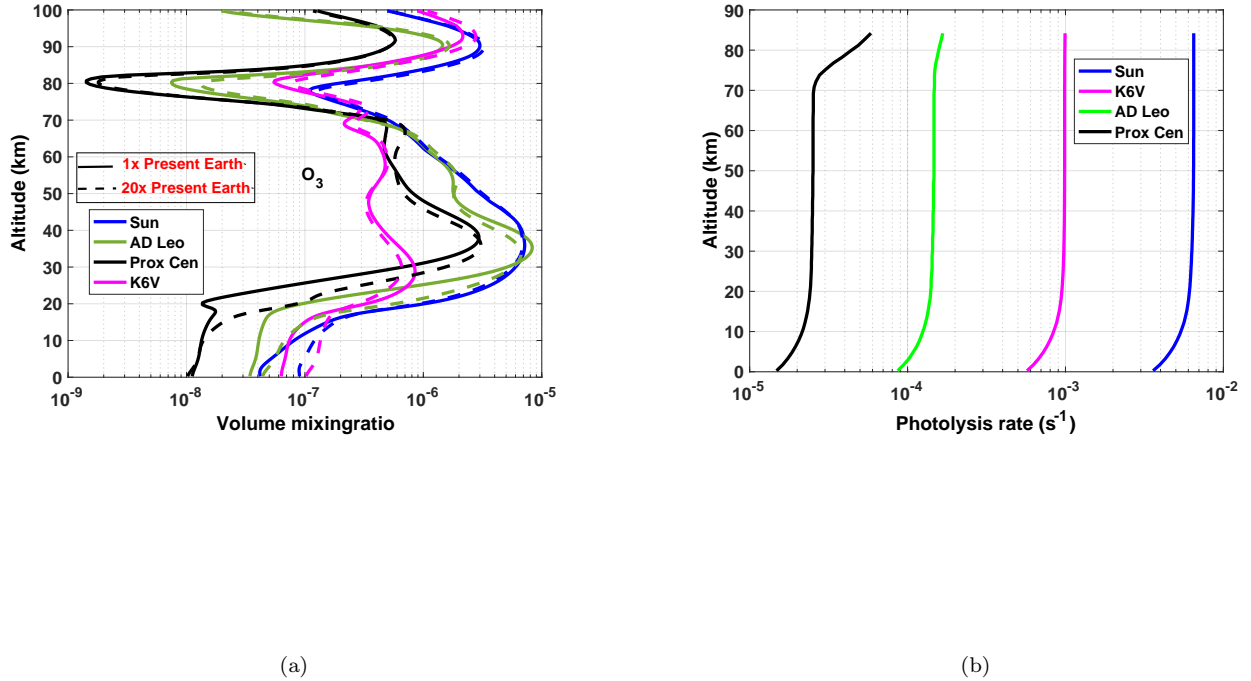


Figure 2. (a): Mixing ratio profiles of O_3 around stars of different spectral types on an Earth-like planet with 1x (solid) and 20x (dashed) present Earth fluxes of NO_2 . Below the troposphere ($\sim < 20\text{km}$), O_3 concentration rapidly increases around a Sun-like star (blue) compared to other star types. Because O_3 is a dominant production mechanism for NO_2 (See Table 1), the concentration of NO_2 ideally should increase. (b) However, as shown in this panel, the photolysis rate of NO_2 increases from the ground to up to 10km - 20km for all star types, as photons of wavelength between $0.29 - 0.42\mu\text{m}$ penetrate into the troposphere. Consequently NO_2 mixing ratio *decreases* between $\sim 10 - 20\text{km}$ (See Fig. 1). Higher than 20km altitude, O_3 dominates the photolysis rate (because NO_2 photolysis is not increasing anymore), and as a result, NO_2 mixing ratio increases as well.

The absorption cross section of NO_2 shows a broad absorption between $0.25-0.6\mu\text{m}$, which has little overlap with absorption from other terrestrial molecular atmospheric constituents (Fig. 3, panel b). The main possible confusion would be related to aerosols with sub-micron sizes ($\sim 0.5\mu\text{m}$), which have absorption features that could mimic the exact same shape as NO_2 . Considering the broad nature of the NO_2 spectral feature, a unique spectroscopic identification will be therefore ultimately challenging, and this investigation solely explores the hypothetical requirements for a possible detection for an absorption due to NO_2 . Other absorption features are also present at $\sim 3.5\mu\text{m}$, $6.4\mu\text{m}$ and $10 - 16\mu\text{m}$, but these overlap with absorption bands from H_2O , CO_2 , and other species (Fig. 3, panel b). In order to assess the detectability of NO_2 as a technosignature, we use the mixing ratio profiles from the 1-D photochemical model as input to the Planetary Spectrum Generator (PSG⁶, Villanueva et al. (2018)) to simulate reflected light, and transit spectra. We estimate the signal-to-noise (SNR) of detecting NO_2 features. PSG is an online radiative transfer suite that integrates the latest radiative transfer methods and spectroscopic parameterizations, and includes a realistic treatment of multiple scattering in layer-by-layer spherical geometry. It can synthesize planetary spectra (atmospheres and surfaces) for a broad range of wavelengths for any given observatory.

⁶ <https://psg.gsfc.nasa.gov/index.php>

Reaction	Integrated reaction/photolysis rate for Sun (s^{-1})	Integrated reaction/photolysis rate for K-dwarf (s^{-1})	Integrated reaction/photolysis rate for 3390K star (s^{-1})	Integrated reaction/photolysis rate for 3000K star (s^{-1})
$CH_3O_2 + NO \rightarrow CH_3O + NO_2$	8.199×10^{10}	8.623×10^{10}	6.850×10^{10}	1.139×10^{10}
$NO + O_3 \rightarrow NO_2 + O_2$	2.919×10^{13}	6.135×10^{12}	2.054×10^{12}	3.868×10^{11}
$NO + O + M \rightarrow NO_2 + M$	7.393×10^9	3.248×10^8	4.515×10^7	1.31×10^6
$NO + HO_2 \rightarrow NO_2 + OH$	5.521×10^{11}	3.1×10^{11}	1.368×10^{11}	4.514×10^{10}
$NO + NO_3 \rightarrow 2NO_2$	1.099×10^{10}	1.387×10^{10}	6.227×10^{10}	3.152×10^{10}
$HO_2NO_2 + M \rightarrow HO_2 + NO_2 + M$	1.713×10^{11}	1.012×10^{12}	1.170×10^{12}	7.157×10^{11}
$NO_3 + h\nu \rightarrow NO_2 + O$	2.949×10^{10}	8.85×10^{10}	1.150×10^{11}	2.974×10^{10}
$NO_2 + O \rightarrow NO + O_2$	2.592×10^{12}	1.0×10^{11}	2.495×10^{11}	2.857×10^{10}
$NO_2 + OH + M \rightarrow HNO_3 + M$	2.512×10^{12}	1.04×10^{10}	1.764×10^8	4.973×10^6
$O + NO_2 \rightarrow NO_3$	1.219×10^{10}	7.234×10^8	5.338×10^8	3.643×10^7
$O_3 + NO_2 \rightarrow NO_3 + O_2$	2.658×10^{10}	1.169×10^{11}	2.014×10^{11}	7.278×10^{10}
$HO_2 + NO_2 + M \rightarrow HO_2NO_2 + M$	1.78×10^{11}	1.017×10^{12}	1.173×10^{12}	7.168×10^{11}
$NO_2 + h\nu \rightarrow NO + O$	2.724×10^{13}	6.43×10^{12}	2.05×10^{12}	4.318×10^{11}

Table 1. Reactions that act as dominant sources and sinks for NO_2 (first column), and column integrated reaction or photolysis rates for an Earth-like planets around Sun (second column), K-dwarf (third column), 3390K star (fourth column) and 3000K star (fifth column). Bold font are production mechanism for NO_2 , and normal font are loss mechanisms. The dominant sink is NO_2 photolysis and the dominant production mechanism is NO reaction with O_3 (in addition to the surface flux).

Species	Sun (molecules/cm ²)	K6V (4715K) (molecules/cm ²)	AD Leo (3390K) (molecules/cm ²)	Proxima (3000K) (molecules/cm ²)
NO_2	4.644×10^{10}	8.589×10^{10}	2.040×10^{11}	2.453×10^{11}
O_3	5.915×10^{13}	2.302×10^{13}	3.217×10^{13}	7.957×10^{12}

Table 2. Column integrated number densities of NO_2 and O_3 (i.e, total number of molecules per unit volume of integrated along a column of atmosphere) on an Earth-like planet with 1x NO_2 flux around stars of different stellar spectral types. NO_2 is more abundant on a planet around cooler stars than around a Sun-like star, despite having more O_3 which is the dominant molecule in producing NO_2 , because short wavelength photons are available more around a Sun-like star than a K or M-dwarf star. This results in higher photolysis rate (destruction) of NO_2 around a Sun-like star (see Table 1) reducing it's abundance .

We performed simulations with PSG to generate reflected light spectra (Fig. 4) of planets around Sun-like star and a K-dwarf star. We then calculated required SNR to detect the NO_2 feature (Fig. 5) between 0.2- 0.7 μm . For these simulations, we assumed a LUVOIR-A like telescope (15 meter) observing with the ECLIPS (Extreme Coronagraph for Living Planetary Systems).⁷ This instrument is an internal coronagraph with the key goal of direct exoplanet observations. It has three channels: NUV (0.2–0.525 μm), visible (0.515–1.030 μm) and NIR (1.0–2.0 μm). The NUV channel is capable of high-contrast imaging only, with an effective spectral resolution of $R \sim 7$. The optical channel contains an imaging camera and integral field spectrograph (IFS) with $R=140$. For our spectral simulations, we use NUV ($R=6$) and visible ($R=70$) channels, as the NO_2 cross section spans from UV into visible wavelengths (See Fig. 3). Because the NO_2 feature is quite broad in the NUV to visible region, a low resolution of $R=6$ and $R=70$ is suffice to resolve the feature, at the same time maximizing the SNR. We calculated wavelength dependent SNR shown in Figs. 4, 5, 6, 7 and 8 as the difference between the spectra with and without the NO_2 feature, divided by the noise

⁷ <https://www.luvoirtelescope.org/>, section 1.11.2, page 75

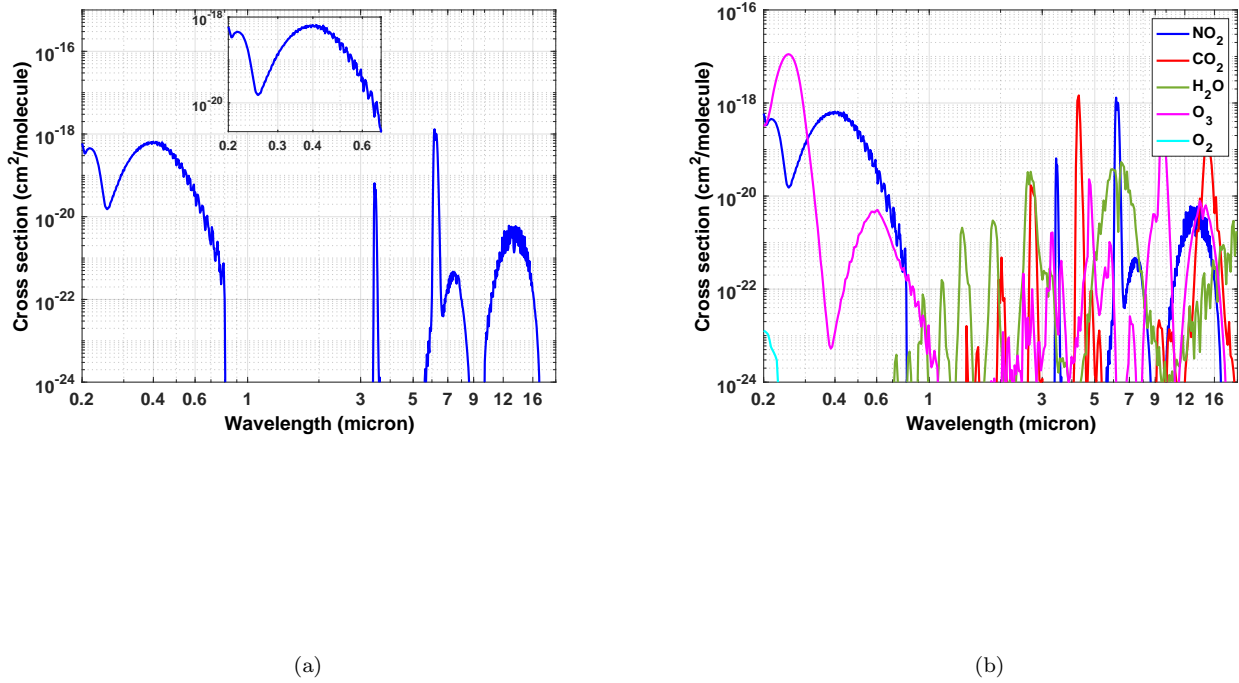


Figure 3. NO_2 absorption cross section as a function of wavelength (panel a). The broad absorption between $0.25\text{--}0.6\ \mu\text{m}$ is the dominant feature, and few other molecules absorb here. The inset figure focuses on the cross section in this wavelength region. Other features in the IR region ($\sim 3.5\ \mu\text{m}$, $6.4\ \mu\text{m}$ and $10\text{--}16\ \mu\text{m}$) are relatively weaker and overlap with absorption from other gas species, in particular H_2O and CO_2 (panel b).

simulated by PSG for the instrument under consideration (see section 5.3 of Villanueva et al. (2018), and also the PSG website⁸ where the noise model is discussed in detail). The “net SNR” is calculated by summing the squares of the individual SNRs at each wavelength within a given band (either NUV or VIS), and then taking the square root. This methodology is largely insensitive to SNR, as long as the feature is resolved by the spectrum. See also Appendix A for a comparison between the PSG coronagraph noise model and a complementary noise model (Robinson et al. 2016; Lustig-Yaeger et al. 2019), showing highly comparable results for the photon count rates and resulting spectral precision. We considered the planets around both the Sun-like and K6V stars to be located at 10 pc distance, residing in the respective habitable zones (HZs) of their host stars as calculated from Kopparapu et al. (2013, 2014), and observed at a phase angle of 45° (0° is secondary eclipse, and 180° is transit). For this feature to be detected, the planet need not be in the HZ, as will be explained later in the discussion section (4).

In both the panels of Fig. 4, the difference of the geometric albedo spectrum with and without NO_2 are shown for different levels scaled by factors of current Earth levels in a 10 hour observation with LUV01R-15m telescope. The corresponding noise is shown as dashed curve. For the Sun-like star (panel a) even very high (20x) concentrations of NO_2 compared to the present Earth levels barely reach the $1 - \sigma$ noise level in the strongest wavelength region. In panel b, increasing the nominal abundance to higher concentrations on a planet around a K-dwarf produces only a marginal improvement over a Sun-like star, with the highest concentration (20x) reaching just above the noise level. This is likely because the column number density of NO_2 on a planet around K-dwarf star seems marginally larger

⁸ <https://psg.gsfc.nasa.gov/helpmodel.php#noise>

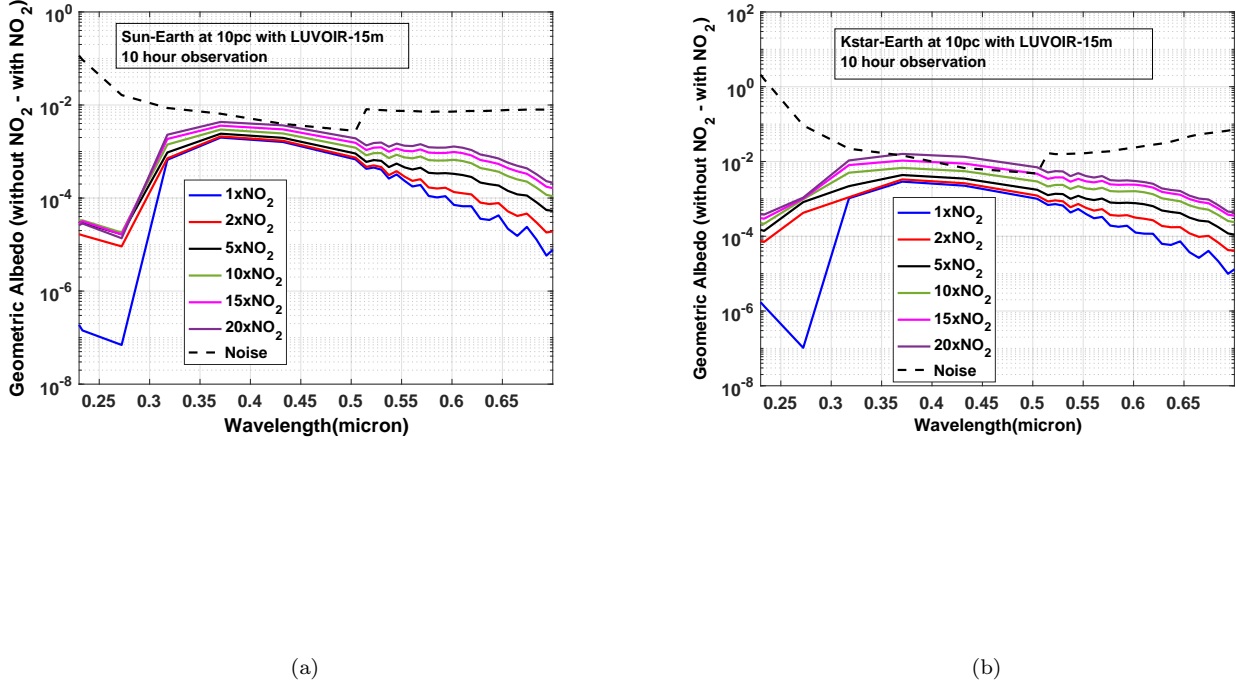


Figure 4. Geometric Albedo difference with and without NO_2 for an Earth-like planet around a Sun-like star (panel a) and around a K6V stellar spectral type (panel b) located at 10 pc with varying NO_2 concentrations, assuming LUVUOIR-A (15 m) observing time of 10 hours. 1σ noise model is also shown (dashed black). The multiple factors in the legend are compared to the concentrations of present Earth level of NO_2 flux (8.64×10^9 molecules/cm²/s) implemented in our photochemical model of an Earth-like planet around each stellar type. These are cloud free model results.

(Table 2) due to less photolysis rate (last row, Table 1). As discussed above, the enhanced NO_2 absorption on the K-dwarf planet compared to the planet around the Sun-like star is driven by the photochemistry.

In Fig. 5, we show the calculated signal to noise ratio (SNR) values of the features shown in Fig. 4 as a function of wavelength for 10 hour exposure times with a LUVUOIR-A like telescope for wavelengths relevant to the NO_2 feature. The “net SNR” indicated in these figures is calculated by summing up the squares of the SNR from each wavelength band and then taking the square-root (see Eq.(6) of Lustig-Yaeger et al. (2019)). Fig. 5(a) shows that for planets around Sun-like stars even an increase of 10x in the NO_2 flux is not enough to detect the feature with any meaningful SNR within 10 hours of observation. Any lower amount of NO_2 would need even more longer observation times.

Fig. 5(b) shows SNR as a function of the same wavelength range for a planet around K-dwarf star. The combined effects of more NO_2 and better planet-star contrast ratio relative to the planet orbiting the Sun (a K6V dwarf is only about one tenth as luminous as a G2V dwarf) makes only a marginal difference in SNR that can be reached in the same time as Sun-like star.

While these SNR may not look promising, there is an interesting question that one can ask and explore an answer: How much LUVUOIR-15 m time is needed to detect present Earth-level concentration of NO_2 around a Sun-like star at 10 pc? Fig.6 (a) shows Geometric albedo spectrum difference with and without NO_2 as a function of wavelength for 300, 600 and 1200 hours of LUVUOIR-A time, respectively. Also shown in dashed lines are the corresponding noise levels for each of these observation times. The present Earth-level NO_2 seems to be well above the noise level after 300 hours of observation time (compare the solid green curve with red-dashed line) indicating that it might be detectable.

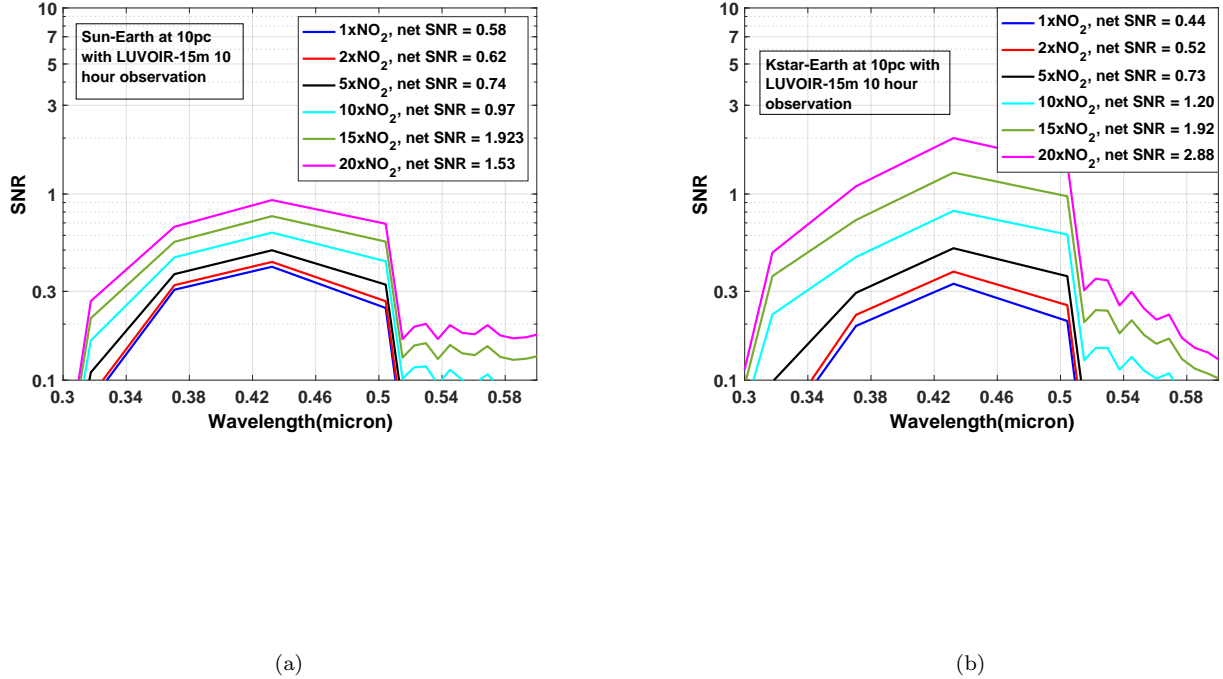


Figure 5. Calculated SNR values to detect various levels of NO₂ concentrations as a function of wavelength, around a Sun-like star (panel a) and for a K6V spectral type star (panel b) located at 10 pc. The calculation assumed a LUVOIR-A (15m) type telescope with 10 hour observation time. While these plots show that at any given wavelength, NO₂ of any concentration is detected comparatively at a higher SNR around a K6V star than a Sun-like star, it will still be challenging to detect the feature within 10 hours. The NO₂ concentrations are generally higher around the K-dwarf star compared to an Earth-like planet around a Sun-like star, giving rise to this marginal increment in SNR around a K-dwarf star. These are cloud free model results.

To find out with what SNR it would be detectable, Fig. 6 (b) shows the “net SNR” to detect present Earth-level NO₂ as a function of observation time. To achieve a net SNR of 5 (dashed red line), it would take LUVOIR-15 m about 400 hours. For comparison, to obtain the Hubble Ultra Deep Field image, ~ 400 hours of actual observation time (~ 1 year in real time) was needed (Beckwith et al. 2006). In fact, Hubble has done even larger programs such as the CANDLES galaxy evolution survey (Grogin et al. 2011) with 902 orbits (~ 900 hours of observation time assuming ~ 1 hour per orbit). This took about 3 years in real time. However, these large programs also obtained data on a huge sample size with thousands of galaxies. LUVOIR is envisaged to be 100% community competed time and the final report of LUVOIR team laid out a DRM in which comparable allocations of time were spent on general astrophysics observations and exoplanet detection and characterization observations during the first 5 years of the mission. So, over the course of the nominal LUVOIR mission lifetime of about 5 years, it may be possible to take data with ~ 400 hour observation time on a prime HZ planet candidate(s) within 10 pc, to potentially obtain a SNR ~ 5 for a present Earth-level NO₂ feature on a Earth-Sun system at 10 pc. An even more interesting aspect is that, we can place upper limits on the amount of NO₂ available on that planet as we spend more observation time on a prime HZ candidate. This could potentially indicate the presence or absence or the level of technological civilization on that planet.

4. DISCUSSION

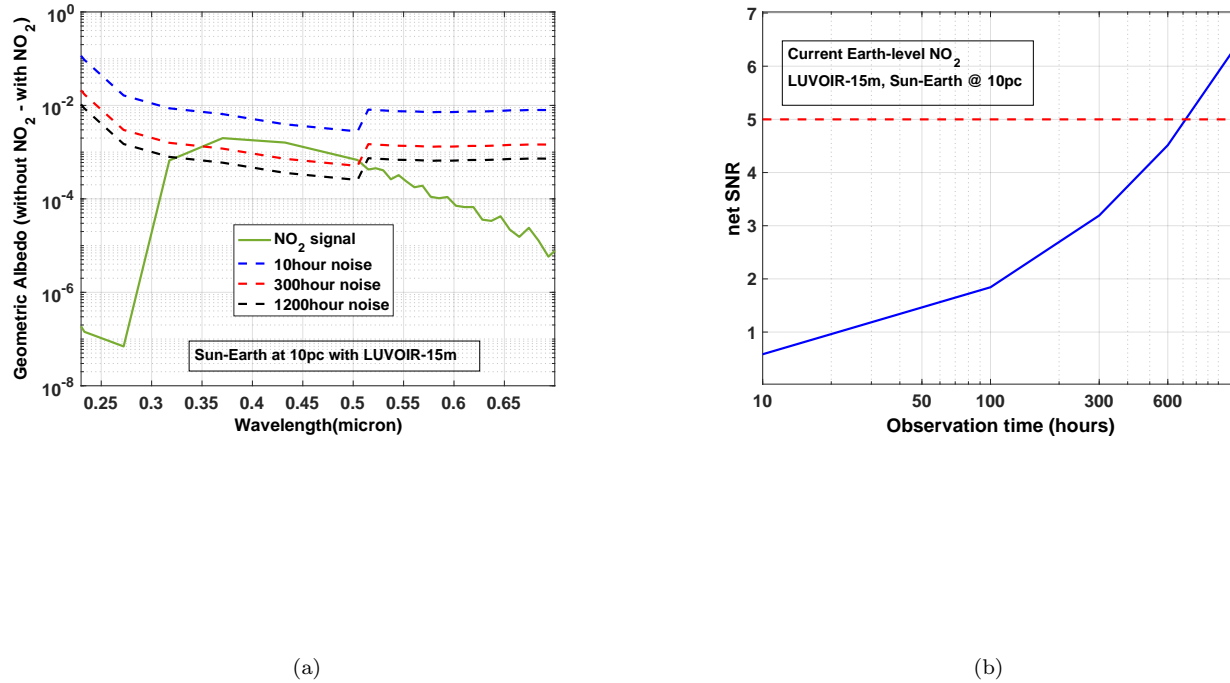


Figure 6. (a) Geometric albedo difference with and without NO₂ as a function of wavelength for different observation times with LUVOIR-15m telescope to detect a present Earth-level NO₂ amount on a Sun-Earth system at 10pc. (b) Integrated SNR (over the wavelengths) versus the amount of observation time needed for the same system configuration. For example, to detect an Earth level NO₂ with SNR ~ 5 (red-dashed line), LUVOIR-15m would need ~ 400 hours of observation time. For comparison, Hubble’s large programs such as the Ultra Deep Field (UDF) and CANDLES surveys used between $\sim 400 - 900$ hours of observation time over a period of 1-3 years. See text for more details.

While the results from the previous section provide a preliminary study of NO₂ as a potential technosignature, some caveats need to be mentioned. First, we have performed 1-D photochemical model calculations using a modern Earth template generated from a 1-D radiative-convective, cloud-free climate model from [Kopparapu et al. \(2013\)](#). Clouds can significantly effect the observed spectrum and potentially alter the calculated SNR. To test this, we have prescribed water-ice clouds (particle size $25\mu\text{m}$) between 0.001 - 0.01bar, and liquid water clouds (particle size $14\mu\text{m}$) between 0.01bar - 0.1bar in PSG. Fig. 7 shows SNR as a function of wavelength for an Earth-like planet around a Sun-like star at 10 pc distance observed with the LUVOIR-15m telescope for 10 hours with (blue solid) and without (red solid) clouds. The absorption cross-sections of water and ice clouds are in the same wavelength region as the peak NO₂ absorption which further masks the NO₂ feature in this band. We should caution that this is all based on ad-hoc prescription of clouds at a certain height, and a more rigorous analysis using 3-D climate models which can simulate self-consistent and time-varying cloud cover need to be performed. We leave that for future study.

Secondly, we have used the 15 m architecture of LUVOIR-A, and the SNR values we report are a best case scenario owing to its large mirror size. Other telescope architectures such as LUVOIR-B (8 m) or HabEX⁹ (a 4 m mirror accompanied by a coronagraph and a starshade) may need more observation time than shown in Fig. 5 and Fig. 7 to detect NO₂ features.

⁹ <https://www.jpl.nasa.gov/habex/pdf/HabEx-Final-Report-Public-Release-LINKED-0924.pdf>

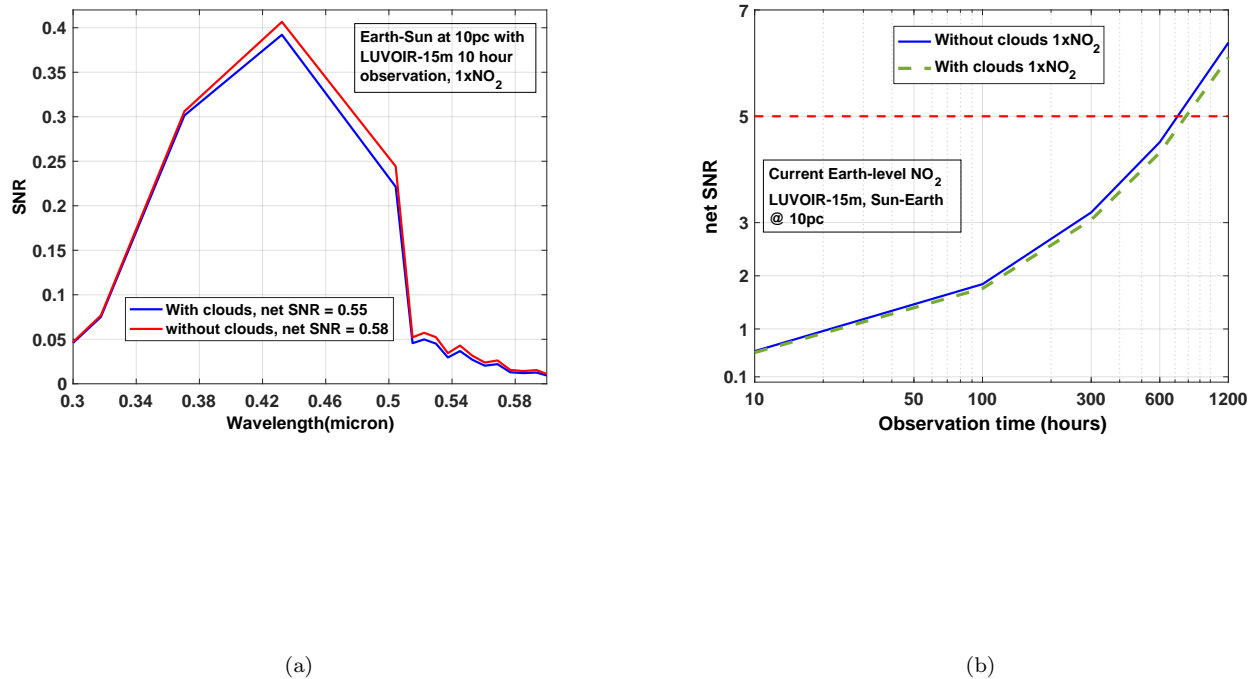


Figure 7. Effect on the SNR of a geometric albedo spectrum with (blue solid) and without (red solid) clouds on an Earth-like planet ($1xNO_2$) around Sun-like star. Water clouds absorb in the same wavelength region as NO_2 absorption bands, thus reducing the SNR and potentially causing confusion source. (b) Similar to Fig.6b, integrated SNR (over the wavelengths) versus the amount of observation time with (green dashed) and without (blue solid) clouds. The time to reach a $SNR = 5$ is slightly longer with clouds.

As shown in Fig. 3, NO_2 also absorbs in the infrared (IR) part of the spectrum, particularly between $3.2-3.7 \mu m$, $5.2-8.9 \mu m$ and $9.7-18 \mu m$. However, the absorption in these regions is either weak across the band compared to the $0.25-0.65 \mu m$ visible band, or limited to a very narrow region of the spectrum. Consequently, detecting NO_2 in transit spectroscopy with either JWST or the flagship mission concept study Origins Space Telescope (OST) would be challenging. Nevertheless, we tested this with PSG, and the results are shown in Fig. 8. We placed a planet like Proxima Cen b around its host star at 10 pc assuming that it transits, with $20x NO_2$ abundance to maximize the signal. We used JWST NIRSpec and OST MISC-Transit instrument for the $\sim 3 \mu m$ and $\sim 6 \mu m$ wavelength regions for the detection of NO_2 . While OST has greater performance than JWST, the observations here are limited by masking features from H_2O and CO_2 in the near-IR. Even at $20x NO_2$ from our photochemical model H_2O features completely dominate the $\sim 6 \mu m$ region of NO_2 absorption (Fig.8(a)). The SNR for a 10 hour and 500 hour observation times for both telescopes is shown in Fig.8(b). Even with large observation times, it would be very challenging to detect the NO_2 feature with any meaningful SNR.

A space-based nulling interferometer such as ESA's LIFE (Large Interferometer for Exoplanets) mission concept (Defrère et al. 2018; Quanz et al. 2018) could potentially detect mid-IR ($5 - 20 \mu m$) features in direct imaging spectra. While we are unable to assess quantitative limits on SNR at this time for this mission, we speculate that phase dependent thermal emission spectroscopy (Wolf et al. 2019; Suissa et al. 2020) may be another way to detect NO_2 feature.

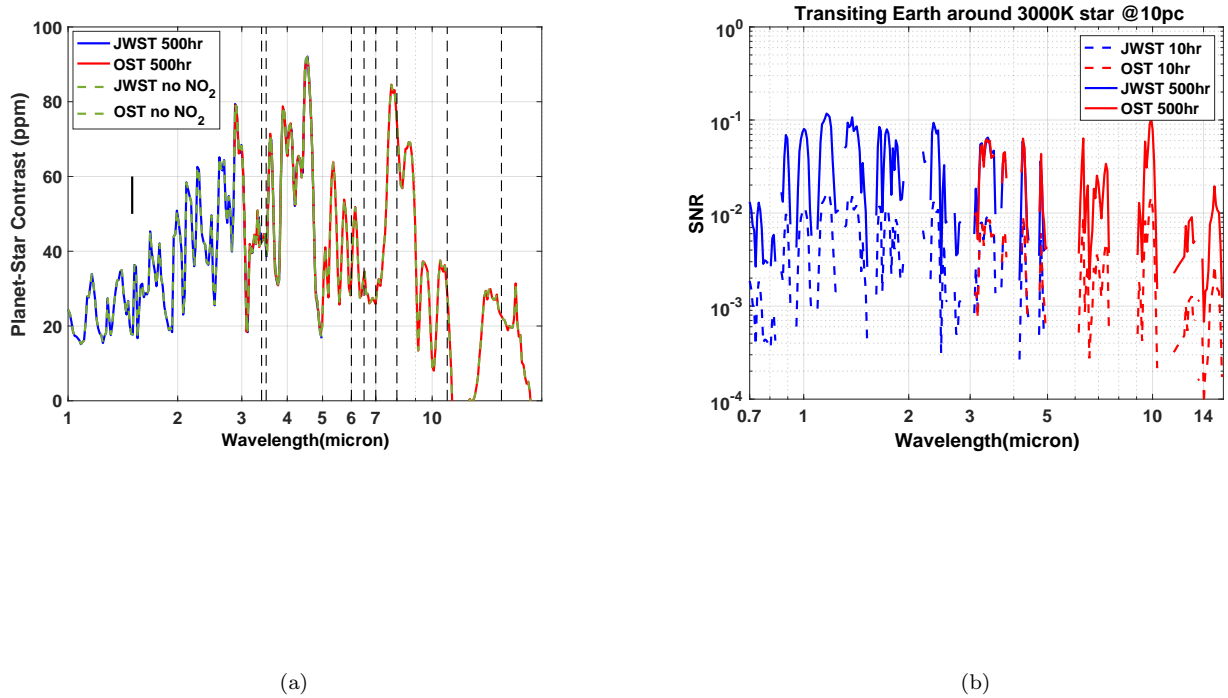


Figure 8. (a) Transit spectrum of NO₂ in the near-IR and mid-IR region on a HZ Earth-like planet around Proxima Cen-like star ($T_{eff} = 3000\text{K}$) located at 10pc with 20x present Earth-level NO₂ fluxes using JWST NIRSpec (blue) and OST MISC (red) observations. No clouds were included. The vertical solid black line indicates the error bar, and dashed lines indicate NO₂ absorption bands in the IR (b) Both 10 hour (dashed) and 500 hour (solid) observations indicate it is very challenging to observe even 20x NO₂ abundance in transit observations in the IR because of several other overlapping gases in this region that have a stronger absorption than NO₂. See Fig. 3(b).

Historically, the United States NO₂ concentrations have varied (gone down) by a factor of 3 over a period of 40 years, from 1980-2019.¹⁰ Therefore, we can expand the possibilities of detecting a technological civilization at the stage where Earth civilization was 40 years ago. It is possible to imagine a more highly industrialized society that could possibly operate in the regime of 5× Earth NO₂ level making it possible to detect it with LUVOIR-15m with even less observation time than for present-Earth conditions. We should stress here that when we mean a technological civilization, it does not necessarily mean a much more advanced society than current Earth level. Just like the search for biosignatures encompass ‘Earth-through time’ with different stages of Earth’s biosphere evolution, we could do a similar search for a ‘technosphere’ at different stages of a technological civilization.

It is possible that atmospheric technosignatures, in particular industrial pollutants like NO₂, are short-lived. However, this is comparable to searches for radio technosignatures where the transient nature of the radio communicative civilizations may also be short-lived. Furthermore, it may be that an industrialized society that is prone to emit NO₂ as a byproduct of their combustion technology may also have radio communication capabilities, just like us. In this respect, a search for radio technosignatures can be performed if NO₂ is detected on a potential habitable planet.

If we are looking for NO₂ as a technosignature, and not as a biosignature, then it may appear that one need not limit the search to known planets in the HZ. A technological civilization can possibly inhabit even an adjacent barren

¹⁰ <https://www.epa.gov/air-trends/nitrogen-dioxide-trends>

planet (like Mars in our Solar System), and use the atmosphere as a waste dump of NO_2 emissions. Or they may prefer to live sub-surface on a HZ planet and release “waste” NO_2 into the atmosphere. Speculations are endless. However, industrial NO_2 on Earth is produced by essentially burning biomass (coal, petroleum products) that have been excavated to fuel the civilization (We note that NO_2 can also be produced by nuclear detonations.) The vast majority of burnable organic matter is directly or indirectly derived from oxygenic photosynthesis, meaning an abiotic or anoxic world would not have abundant preserved organic matter. To burn this biomass, one needs an atmosphere with oxygen. The observation of high abundances of NO_2 on an exoplanet atmosphere would indicate a sustained source of industrial production, likely requiring an oxic atmosphere and indicating a significant source of biomass to sustain long-term industrial activity. While NO_2 can exist in abundant quantities on planets around K-dwarf stars, it may not necessarily be a desirable thing for the inhabitants if they have biology similar to humans, because exposure to NO_2 could cause impairment of lung function and/or recurrent respiratory problems (Faustini et al. 2014b). Conversely, if extraterrestrial biology is sufficiently different from Earth life, then it could be impervious to NO_2 toxicity. In this respect, NO_2 on K-dwarfs is similar to the likely accumulation of abiotic and biologically produced CO on Earth-like planets orbiting mid-to-late M-dwarfs, in addition to the accumulation of biosignature gases (Schwieterman et al. 2019).

Missions like LUVOIR, HabEX, and OST may have biosignature targets as a priority, so it may be untenable to seek dedicated observing time for exclusive technosignature detection. However, in the search for exo-Earth candidates, we will undoubtedly detect other planets within the stellar system (Stark et al. 2014; Kopparapu et al. 2018). LUVOIR and HabEX will be able to simultaneously obtain the spectra of the other bright planets in the system, while performing their observations on a prime HZ target. Consequently, there may not be a need to schedule separate observation time for technosignature detection, as such efforts could “piggy back” on a routine survey to observe both HZ and non-HZ planets (Lingam & Loeb 2019). However, this assumes that the NO_2 detection will likely occur within the total integrated observational time spent on the prime HZ candidate for the biosignature detection, whereas Fig. 5 indicates lower NO_2 abundances may require longer search times.

5. CONCLUSION

The presence of NO_2 on Earth today results in part from sustained industrial processes in urban areas. This paper suggests that the detection of NO_2 in an exoplanet atmosphere could serve as a technosignature, as Earth-level biogenic sources would be unable to generate detectable atmospheric abundances of NO_2 . Using a 1-D photochemical model that uses present Earth atmospheric temperature profile, we find that it would be challenging to detect Earth-level NO_2 around G and K-dwarf stars through direct imaging with only 10 hours of observation time. To detect present Earth-level NO_2 concentration with a SNR ~ 5 , it would take ~ 400 hours of LUVOIR-15m telescope. Such large programs may be possible considering several hundred hours of observing time spent on Hubble UDF and CANDLES surveys. Historically, the United States NO_2 emission varied (gone down) by roughly a factor of ~ 3 over 40 years from 1980-2019. Hence, there might be a possibility to detect 40-year old Earth-level industrialized society with even less time. In this cloud free model, habitable planets orbiting K-dwarf stars, by comparison, would marginally need less amount of time to detect present-day NO_2 abundance. The advantage of searching K-dwarf planets has already been noted in the search for biosignatures (Cuntz & Guinan 2016; Arney 2019), and our results indicate that K-dwarf planets could similarly be advantageous when searching for technosignatures like NO_2 .

However, when we prescribe water-ice and liquid water clouds, there is a moderate decrease in the SNR of the geometric albedo spectrum from LUVOIR-15 m, with present Earth-level NO_2 concentration on an Earth-like planet around a Sun-like star at 10 pc. Clouds and aerosols can reduce the detectability and could mimic the NO_2 feature, posing a challenge to the unique identification of this signature. This highlights the need for performing these calculations with a 3-D climate model which can simulate variability of the cloud cover and atmospheric dynamics self-consistently.

While NO_2 absorbs even in the near-IR and mid-IR, we find that transit observations in this region with JWST and OST may prove challenging to detect NO_2 because of the weaker absorption and also due to overlapping gas absorption of potent greenhouse gases such as H_2O , CO_2 and CH_4 .

Further work is needed to explore the detectability of NO_2 on Earth-like planets around M-dwarfs in direct imaging observations in the near-IR with ground-based 30 m class telescopes. NO_2 concentrations increase on planets around cooler stars due to reduced availability of short-wavelength photons that can photolyze NO_2 . Non-detectability at

longer observation times could place upper limits on the amount NO_2 present on M-dwarf HZ planets like Prox Cen b.

The serendipitous detection of NO_2 , or any other potential artificial atmospheric spectral signature (CFCs, for example) may become a watershed event in the search for life (biological or technological). Is it likely that biosignatures are more prevalent than technosignatures? We will not know for certain until we search. Our aim in this study is to point out that both biosignatures and technosignatures are two sides of the same coin, and the search for both can co-exist together with upcoming observatories. It is worth pointing out the obvious in this concluding statement: the question “Are we alone?”—which has been the driving force behind the search for extraterrestrial biosignatures—is a question posed by a technological civilization.

ACKNOWLEDGMENTS

The authors would like to thank an anonymous reviewer whose comments greatly improved the manuscript. We would also like to thank Sandra Bastelberger, Chester “Sonny” Harman, Thomas Fauchez, James Kasting and Avi Mandell for discussions that helped in this work. R. K. would like to acknowledge Vivaswan Kopparapu, his 11 year old son, who helped R. K. to realize that increasing the LUVOIR-15m observation time by a factor of 4 doubles the NO_2 SNR for an Earth-Sun system at 10 pc. Goddard affiliates acknowledge support from the GSFC Sellers Exoplanet Environments Collaboration (SEEC), which is supported by NASA’s Planetary Science Division’s Research Program. J.H.M. gratefully acknowledges support from the NASA Exobiology program under grant 80NSSC20K0622. This work was performed as part of NASA’s Virtual Planetary Laboratory, supported by the National Aeronautics and Space Administration through the NASA Astrobiology Institute under solicitation NNH12ZDA002C and Cooperative Agreement Number NNA13AA93A, and by the NASA Astrobiology Program under grant 80NSSC18K0829 as part of the Nexus for Exoplanet System Science (NExSS) research coordination network.

APPENDIX

A. COMPARISON OF LUVOIR NOISE MODELS

We conducted a comparison between the LUVOIR coronagraph noise model included in PSG and the Python implementation of the [Robinson et al. \(2016\)](#) coronagraph noise model from [Lustig-Yaeger et al. \(2019\)](#) (henceforth CG). We found the two models to agree very well (Figure 10), with both models implementing very similar formalisms for computing sensitivities.

We define the end-to-end throughput for the planetary fluxes as: $T_{total} = T_{Tele} \times T_{cor} \times T_{opt} \times T_{read} \times T_{QE}$, where T_{Tele} accounts for light lost due to contamination and inefficiencies in the main collecting area, T_{cor} is the coronagraphic throughput at this planet-star separation, T_{opt} is the optical throughput (the transmissivity of all optics), T_{QE} is the raw quantum efficiency (QE) of the detector, and T_{read} is the read-out efficiencies. The left panel in Figure 9 shows the optical throughput (T_{opt}) from [Stark et al. \(2019\)](#) and the right panel shows the coronagraph throughput as a function of planet-star separation (T_{cor}). Although the design of the LUVOIR-A coronagraph has multiple different masks with slightly different IWAs, both coronagraph models use a combined mask (shown in Figure 9) to approximate the optimal use of the coronagraph for any simulated target. Importantly, the coronagraph throughput already accounts for the fraction of the exoplanetary light that falls within the photometric aperture, denoted f_{pa} in [Robinson et al. \(2016\)](#), so we manually set $f_{pa} = 1$ in the CG model to properly account for this factor. The number of stellar photons is defined by the contrast at the core throughput, and thus the number of stellar photons is calculated as $C \cdot \max(T_{cor}) \approx 10^{-10} \cdot 0.27$. For T_{Tele} , we adopt 0.95 for all wavelengths, on par with the particulate coverage fraction for JWST’s mirrors. EMCCD detectors are expected to have T_{read} near 0.75 ([Stark et al. 2019](#)), while for NIR and other detectors, read-out inefficiencies and bad-pixels may account to a similar value, and we adopt $T_{read}=0.75$ across all detectors as a conservative estimate. The reported quantum efficiency of the different detectors ranges from 0.6 to 0.9, yet technological improvements in several of these detectors could be expected in the near future, and we adopt a general $T_{QE}=0.9$ for all detectors.

The Signal-to-Noise ratio (SNR) is effectively defined by the different sources of noise, quantified as count rates. We not only compared resulting SNRs between the two models, but also the simulated count rates for the different

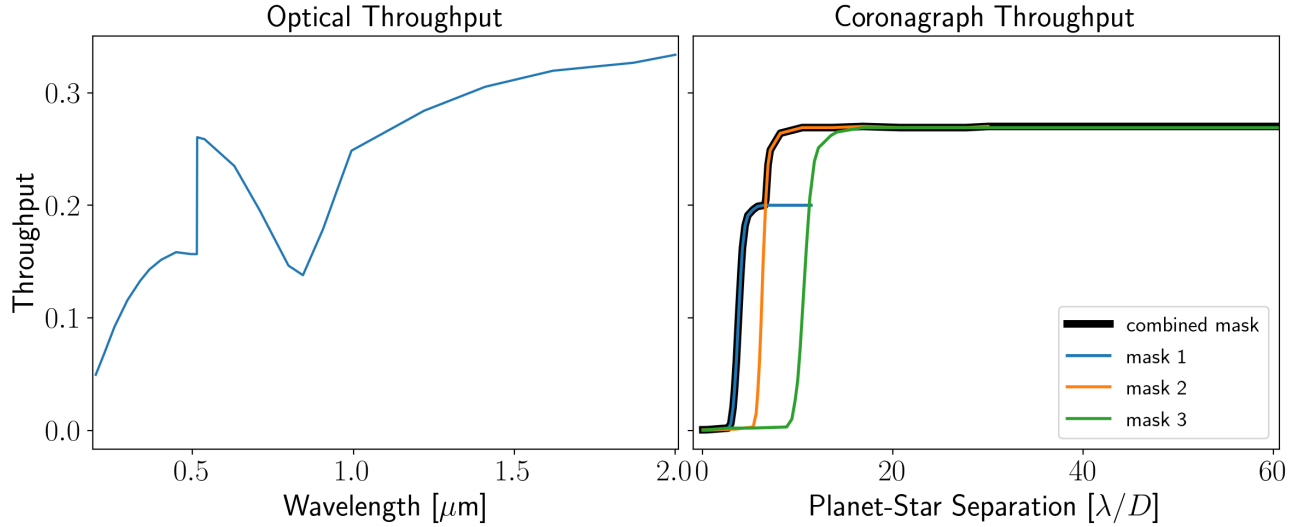


Figure 9. Coronagraph throughputs used for LUVOIR-A noise modeling. The left panel shows the wavelength dependent optical throughput. The right panel shows the coronagraph throughput as a function of planet-star separation.

Table 3. LUVOIR-A coronagraph model input parameters

Parameter	Description	Value
D	Mirror Diameter	15 m
C	Contrast	10^{-10}
T_{opt}	Optical Throughput	Figure 9 (left)
T_{cor}	Coronagraph Throughput	Figure 9 (right)
R_{e-}	Read Noise (UVIS/NIR)	0 / 2.5
D_{e-}	Dark Current (UVIS/NIR)	$3E-5 / 2E-3 \text{ s}^{-1}$
X	Circular Photometric Aperture Radius	$0.61\lambda/D$
N_{ez}	Number of Exozodis	4.5

components, and found very good agreement (Figure 10). For these simulations, we assumed a circular aperture defined by diffraction ($1.22 \lambda/D$), an exo-zodiacal level of 4.5 times the one of our solar system (22 mag/arcsec^2), and a local zodi level of $22.5 \text{ mag/arcsec}^2$. The noise term was computed as

$$C_{noise} = \sqrt{C_p + C_s + 2C_b} \quad (\text{A1})$$

where C_p is the total number of planet photons, C_s is the stellar photon noise (e.g. “leakage” through the coronagraph), and C_b is the total background, which includes all other noise sources such as zodi, exozodi, dark current, thermal, and read noise. Observations are normally performed as on-off, meaning one with the planet, and one without. As such, the background sources of noise need to be counted twice (equation A1). Depending on the observational procedure, the stellar photons can be assumed to be present in the “off” position or not. Robinson et al. (2016) assumes by default that the star is also in the “off” position, and therefore doubles C_s , while the default in PSG is the “off” position without star leakage (so only counted once, equation A1). We explored the impact on the SNR of this assumption in the observational procedure, and only observe small ($<10\%$) differences in the resulting SNR (Figure 10).

REFERENCES

- Arney, G., Domagal-Goldman, S. D., Meadows, V. S., et al. 2016, *Astrobiology*, 16, 873, doi: [10.1089/ast.2015.1422](https://doi.org/10.1089/ast.2015.1422)
- Arney, G. N. 2019, *ApJL*, 873, L7, doi: [10.3847/2041-8213/ab0651](https://doi.org/10.3847/2041-8213/ab0651)

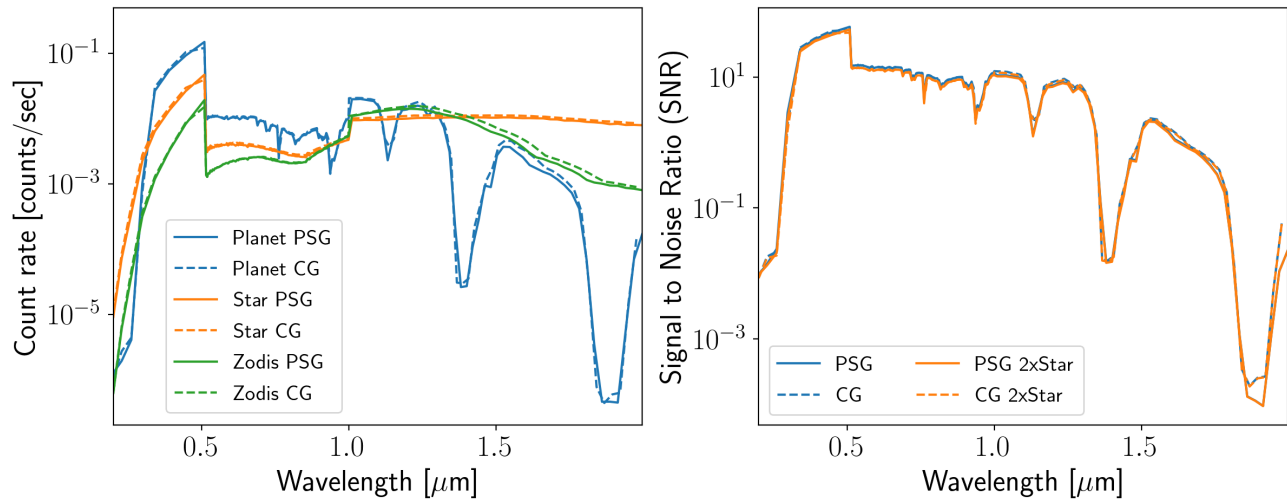


Figure 10. Comparison between PSG and CG for LUVOIR-A. Left: photon count rates for the planet signal and dominant noise sources. Right: Precision on the visible spectrum in a 10 hour exposure for PSG and CG. The 2xStar values present the case in which star leakage is also considered in the “off” position. Both panels were computed assuming the native spectral resolutions of the channels (RP=7/140/70 for UV/VIS/NIR respectively).

Arnold, L. 2005, *\apj*, 627, 534, doi: [10.1086/430437](https://doi.org/10.1086/430437)
 Bauwens, M., Compennolle, S., Stavrakou, T., et al. 2020, *Geophysical Research Letters*, e2020GL087978
 Beckwith, S. V., Stiavelli, M., Koekemoer, A. M., et al. 2006, *The Astronomical Journal*, 132, 1729
 Benneke, B., Wong, I., Piaulet, C., et al. 2019, *ApJL*, 887, L14, doi: [10.3847/2041-8213/ab59dc](https://doi.org/10.3847/2041-8213/ab59dc)
 Bracewell, R. N. 1960, *Nature*, 186, 670, doi: [10.1038/186670a0](https://doi.org/10.1038/186670a0)
 Carrigan Jr., R. 2009, in *Astronomical Society of the Pacific Conference Series*, Vol. 420, *Bioastronomy 2007: Molecules, Microbes and Extraterrestrial Life*, ed. K. Meech, J. Keane, M. Mumma, J. Siefert, & D. Werthimer, 415
 Catling, D. C., Krissansen-Totton, J., Kiang, N. Y., et al. 2018, *Astrobiology*, 18, 709, doi: [10.1089/ast.2017.1737](https://doi.org/10.1089/ast.2017.1737)
 Chance, K., & Kurucz, R. L. 2010, *JQSRT*, 111, 1289, doi: [10.1016/j.jqsrt.2010.01.036](https://doi.org/10.1016/j.jqsrt.2010.01.036)
 Charbonneau, D., Brown, T. M., Noyes, R. W., & Gilliland, R. L. 2002, *ApJ*, 568, 377, doi: [10.1086/338770](https://doi.org/10.1086/338770)
 Crutzen, P. J. 2006, in *Earth system science in the anthropocene* (Springer), 13–18
 Cuntz, M., & Guinan, E. 2016, *The Astrophysical Journal*, 827, 79
 DeFrère, D., Léger, A., Absil, O., et al. 2018, *Experimental Astronomy*, 46, 543, doi: [10.1007/s10686-018-9613-2](https://doi.org/10.1007/s10686-018-9613-2)
 Domagal-Goldman, S. D., Segura, A., Claire, M. W., Robinson, T. D., & Meadows, V. S. 2014, *ApJ*, 792, 90, doi: [10.1088/0004-637X/792/2/90](https://doi.org/10.1088/0004-637X/792/2/90)
 Dyson, F. J. 1960, *Science*, 131, 1667, doi: [10.1126/science.131.3414.1667](https://doi.org/10.1126/science.131.3414.1667)

Faustini, A., Rapp, R., & Forastiere, F. 2014a, *European Respiratory Journal*, 44, 744
 —. 2014b, *European Respiratory Journal*, 44, 744
 Forgan, D. 2013, *Journal of the British Interplanetary Society*, 66, 144
 France, K., Loyd, R. O. P., Youngblood, A., et al. 2016, *ApJ*, 820, 89, doi: [10.3847/0004-637X/820/2/89](https://doi.org/10.3847/0004-637X/820/2/89)
 Frank, A., Kleidon, A., & Alberti, M. 2017, *Anthropocene*, 19, 13
 Freitas Jr, R. A., & Valdes, F. 1980, *Icarus*, 42, 442
 Fujii, Y., Angerhausen, D., Deitrick, R., et al. 2018, *Astrobiology*, 18, 739, doi: [10.1089/ast.2017.1733](https://doi.org/10.1089/ast.2017.1733)
 Grenfell, J. L. 2017, *Physics Reports*, 713, 1
 Grogin, N. A., Kocevski, D. D., Faber, S. M., et al. 2011, *ApJS*, 197, 35, doi: [10.1088/0067-0049/197/2/35](https://doi.org/10.1088/0067-0049/197/2/35)
 Haqq-Misra, J., & Kopparapu, R. K. 2012, *Acta Astronautica*, 72, 15, doi: [10.1016/j.actaastro.2011.10.010](https://doi.org/10.1016/j.actaastro.2011.10.010)
 Haqq-Misra, J., Kopparapu, R. K., & Schwieterman, E. 2020, *Astrobiology*, 20, 572, doi: [10.1089/ast.2019.2154](https://doi.org/10.1089/ast.2019.2154)
 Harman, C. E., Felton, R., Hu, R., et al. 2018, *ApJ*, 866, 56, doi: [10.3847/1538-4357/aadd9b](https://doi.org/10.3847/1538-4357/aadd9b)
 Harman, C. E., Schwieterman, E. W., Schottelkotte, J. C., & Kasting, J. F. 2015, *ApJ*, 812, 137, doi: [10.1088/0004-637X/812/2/137](https://doi.org/10.1088/0004-637X/812/2/137)
 Holmes, C. D., Prather, M. J., Søvde, O. A., & Myhre, G. 2013, *Atmospheric Chemistry and Physics*, 13, 285, doi: [10.5194/acp-13-285-2013](https://doi.org/10.5194/acp-13-285-2013)
 Kaltenecker, L. 2017, *Annual Review of Astronomy and Astrophysics*, 55, 433
 Kasting, J., & Ackerman, T. 1985, *Journal of atmospheric chemistry*, 3, 321

- Kasting, J. F., Liu, S. C., & Donahue, T. M. 1979, *J. Geophys. Res.*, 84, 3097, doi: [10.1029/JC084iC06p03097](https://doi.org/10.1029/JC084iC06p03097)
- Kipping, D., & Teachey, A. 2016, *\mnras*, 459, 1233, doi: [10.1093/mnras/stw672](https://doi.org/10.1093/mnras/stw672)
- Kopparapu, R. k., Kasting, J. F., & Zahnle, K. J. 2012, *ApJ*, 745, 77, doi: [10.1088/0004-637X/745/1/77](https://doi.org/10.1088/0004-637X/745/1/77)
- Kopparapu, R. K., Ramirez, R. M., SchottelKotte, J., et al. 2014, *ApJL*, 787, L29, doi: [10.1088/2041-8205/787/2/L29](https://doi.org/10.1088/2041-8205/787/2/L29)
- Kopparapu, R. K., Ramirez, R., Kasting, J. F., et al. 2013, *ApJ*, 765, 131, doi: [10.1088/0004-637X/765/2/131](https://doi.org/10.1088/0004-637X/765/2/131)
- Kopparapu, R. K., Hébrard, E., Belikov, R., et al. 2018, *ApJ*, 856, 122, doi: [10.3847/1538-4357/aab205](https://doi.org/10.3847/1538-4357/aab205)
- Kraus, A., & Hofzumahaus, A. 1998, in *Atmospheric Measurements during POPCORN—Characterisation of the Photochemistry over a Rural Area* (Springer), 161–180
- Krissansen-Totton, J., Olson, S., & Catling, D. C. 2018, *Science Advances*, 4, eaao5747, doi: [10.1126/sciadv.aao5747](https://doi.org/10.1126/sciadv.aao5747)
- Kuhn, J. R., & Berdyugina, S. V. 2015, *International journal of astrobiology*, 14, 401
- Lammer, H., Sproß, L., Grenfell, J. L., et al. 2019, *Astrobiology*, 19, 927
- Lamsal, L., Martin, R., Parrish, D., & Krotkov, N. 2013, *Environmental science & technology*, 47, 7855
- Lewis, S. L., & Maslin, M. A. 2015, *Nature*, 519, 171
- Lin, H. W., Gonzalez Abad, G., & Loeb, A. 2014, *ApJL*, 792, L7, doi: [10.1088/2041-8205/792/1/L7](https://doi.org/10.1088/2041-8205/792/1/L7)
- Lincowski, A. P., Meadows, V. S., Crisp, D., et al. 2018, *ApJ*, 867, 76, doi: [10.3847/1538-4357/aae36a](https://doi.org/10.3847/1538-4357/aae36a)
- Lingam, M., & Loeb, A. 2017, *\mnras*, 470, L82, doi: [10.1093/mnrasl/slx084](https://doi.org/10.1093/mnrasl/slx084)
- Lingam, M., & Loeb, A. 2019, *Astrobiology*, 19, 28, doi: [10.1089/ast.2018.1936](https://doi.org/10.1089/ast.2018.1936)
- Loeb, A., & Turner, E. 2012, *Astrobiology*, 12, 290, doi: [10.1089/ast.2011.0758](https://doi.org/10.1089/ast.2011.0758)
- Loyd, R. O. P., France, K., Youngblood, A., et al. 2016, *ApJ*, 824, 102, doi: [10.3847/0004-637X/824/2/102](https://doi.org/10.3847/0004-637X/824/2/102)
- Lustig-Yaeger, J., Meadows, V. S., & Lincowski, A. P. 2019, *AJ*, 158, 27, doi: [10.3847/1538-3881/ab21e0](https://doi.org/10.3847/1538-3881/ab21e0)
- Lustig-Yaeger, J., Robinson, T., & Arney, G. 2019, *Journal of Open Source Software*, 4, 1387, doi: [10.21105/joss.01387](https://doi.org/10.21105/joss.01387)
- Meadows, V. S., Reinhard, C. T., Arney, G. N., et al. 2018, *Astrobiology*, 18, 630, doi: [10.1089/ast.2017.1727](https://doi.org/10.1089/ast.2017.1727)
- Meadows, V. S., Arney, G. N., Schwieterman, E. W., et al. 2018, *Astrobiology*, 18, 133
- O'Malley-James, J. T., & Kaltenegger, L. 2019, *The Astrophysical Journal Letters*, 879, L20
- Pallé, E. 2018, *The Detectability of Earth's Biosignatures Across Time*, 70, doi: [10.1007/978-3-319-55333-7_70](https://doi.org/10.1007/978-3-319-55333-7_70)
- Quanz, S. P., Kammerer, J., Defrère, D., et al. 2018, in *Society of Photo-Optical Instrumentation Engineers (SPIE) Conference Series*, Vol. 10701, *Optical and Infrared Interferometry and Imaging VI*, 107011I, doi: [10.1117/12.2312051](https://doi.org/10.1117/12.2312051)
- Ranjan, S., Schwieterman, E. W., Harman, C., et al. 2020, *ApJ*, 896, 148, doi: [10.3847/1538-4357/ab9363](https://doi.org/10.3847/1538-4357/ab9363)
- Robinson, T. D., Stapelfeldt, K. R., & Marley, M. S. 2016, *PASP*, 128, 025003, doi: [10.1088/1538-3873/128/960/025003](https://doi.org/10.1088/1538-3873/128/960/025003)
- Rose, C., & Wright, G. 2004, *Nature*, 431, 47, doi: [10.1038/nature02884](https://doi.org/10.1038/nature02884)
- Schneider, J. 2010, *Astrobiology*, 10, 857, doi: [10.1089/ast.2010.9499](https://doi.org/10.1089/ast.2010.9499)
- Schwieterman, E. W., Reinhard, C. T., Olson, S. L., Harman, C. E., & Lyons, T. W. 2019, *ApJ*, 878, 19, doi: [10.3847/1538-4357/ab1d52](https://doi.org/10.3847/1538-4357/ab1d52)
- Schwieterman, E. W., Kiang, N. Y., Parenteau, M. N., et al. 2018, *Astrobiology*, 18, 663, doi: [10.1089/ast.2017.1729](https://doi.org/10.1089/ast.2017.1729)
- Seager, S., Schrenk, M., & Bains, W. 2012, *Astrobiology*, 12, 61
- Segura, A., Kasting, J. F., Meadows, V., et al. 2005, *Astrobiology*, 5, 706, doi: [10.1089/ast.2005.5.706](https://doi.org/10.1089/ast.2005.5.706)
- Shklovskii, I. S., & Sagan, C. 1966, *Intelligent life in the universe: Vselennaja zizn'razum*, Delta-books (Holden-Day).
<https://books.google.com/books?id=o4cRAQAIAAJ>
- Stark, C. C., Roberge, A., Mandell, A., & Robinson, T. D. 2014, *ApJ*, 795, 122, doi: [10.1088/0004-637X/795/2/122](https://doi.org/10.1088/0004-637X/795/2/122)
- Stark, C. C., Belikov, R., Bolcar, M. R., et al. 2019, *Journal of Astronomical Telescopes, Instruments, and Systems*, 5, 1, doi: [10.1117/1.JATIS.5.2.024009](https://doi.org/10.1117/1.JATIS.5.2.024009)
- Stevens, A., Forgan, D., & James, J. 2016, *International Journal of Astrobiology*, 15, 333, doi: [10.1017/S1473550415000397](https://doi.org/10.1017/S1473550415000397)
- Suissa, G., Wolf, E. T., Kopparapu, R. k., et al. 2020, *arXiv e-prints*, arXiv:2001.00955.
<https://arxiv.org/abs/2001.00955>
- Technosignatures Workshop Participants, N. 2018, *arXiv e-prints*, arXiv:1812.08681.
<https://arxiv.org/abs/1812.08681>
- Tsiaras, A., Waldmann, I. P., Tinetti, G., Tennyson, J., & Yurchenko, S. N. 2019, *Nature Astronomy*, 3, 1086, doi: [10.1038/s41550-019-0878-9](https://doi.org/10.1038/s41550-019-0878-9)
- Villanueva, G. L., Smith, M. D., Protopapa, S., Faggi, S., & Mandell, A. M. 2018, *JQSRT*, 217, 86, doi: [10.1016/j.jqsrt.2018.05.023](https://doi.org/10.1016/j.jqsrt.2018.05.023)

- Walker, S. I., Bains, W., Cronin, L., et al. 2018, *Astrobiology*, 18, 779, doi: [10.1089/ast.2017.1738](https://doi.org/10.1089/ast.2017.1738)
- Whitmire, D., & Wright, D. 1980, *Icarus*, 42, 149, doi: [10.1016/0019-1035\(80\)90253-5](https://doi.org/10.1016/0019-1035(80)90253-5)
- Wolf, E. T., Kopparapu, R. K., & Haqq-Misra, J. 2019, *ApJ*, 877, 35, doi: [10.3847/1538-4357/ab184a](https://doi.org/10.3847/1538-4357/ab184a)
- Wright, J. T. 2019, arXiv e-prints, arXiv:1907.07832. <https://arxiv.org/abs/1907.07832>
- Wright, J. T., Cartier, K. M. S., Zhao, M., Jontof-Hutter, D., & Ford, E. B. 2016, *ApJ*, 816, 17, doi: [10.3847/0004-637X/816/1/17](https://doi.org/10.3847/0004-637X/816/1/17)
- Wright, J. T., Griffith, R. L., Sigurdsson, S., Povich, M. S., & Mullan, B. 2014, *ApJ*, 792, 27, doi: [10.1088/0004-637X/792/1/27](https://doi.org/10.1088/0004-637X/792/1/27)
- Youngblood, A., France, K., Loyd, R. O. P., et al. 2016, *ApJ*, 824, 101, doi: [10.3847/0004-637X/824/2/101](https://doi.org/10.3847/0004-637X/824/2/101)